Hindawi Publishing Corporation
EURASIP Journal on Advances in Signal Processing
Volume 2008, Article ID 328041, 15 pages
doi:10.1155/2008/328041

Research Article

Pruned Multiangle Resolution Fast Beamforming

Yeo-Sun Yoon,[1,2] Lance M. Kaplan,[3] Seung-Mok Oh,[4] and James H. McClellan[5]

[1] *Center for Advanced Communications, Villanova University, Villanova, PA 19085, USA*
[2] *Radar System Group, Samsung Thales Company, Yongin, Kyunggido, Korea*
[3] *Army Research Laboratory, Adelphi, MD 20783, USA*
[4] *Texas Instruments, Inc. San Diego, CA 92121, USA*
[5] *Center for Signal and Image Processing (CSIP), School of Electrical and Computer Engineering, Georgia Institute of Technology, Atlanta, GA 30332, USA*

Correspondence should be addressed to Yeo-Sun Yoon, ysyoon@ieee.org

Received 8 June 2007; Accepted 23 March 2008

Recommended by Bernhard Wess

Delay-and-sum (DS) beamforming is a simple processing method that can estimate the direction-of-arrival from multiple signal sources. The major advantage of DS beamforming is that it can handle wideband as well as narrowband signals. However, DS beamforming exhibits high computational complexity. The multiangle resolution fast beamformer was proposed as a computationally efficient approximation of DS beamforming, reducing the computational order of complexity from $O(n^3)$ to $O(n^2 \log n)$. In this paper, we introduce the *pruned* multiangle resolution fast beamformer to further reduce the computational complexity. The new algorithm includes an energy detector at intermediate stages of the fast beamformer to prune sectors that do not exhibit increasing energy consistent with coherent integration. Simulations are provided to assess the performance of the pruned fast beamformer. One use for the estimates from the pruned fast beamformer is to initialize high-resolution direction-of-arrival (DOA) estimators such as coherent signal subspace methods.

1. INTRODUCTION

Directional-of-arrival (DOA) estimators are essential for target surveillance and modern communication systems. These algorithms estimate the DOA of signal sources by incorporating measurements from multiple sensors forming an array. While there are many DOA estimators such as MUSIC [1] or ESPRIT [2] for narrowband signals, there are only a few DOA estimators for wideband signal sources. Many narrowband DOA estimators exploit the fact that the time-delay maps into a phase shift [3], but these algorithms are not applicable to wideband signals where different DOAs do not generate simple phase shifts. Delay-and-sum (DS) beamforming is a time-domain algorithm that determines DOAs by coherently summing the energy in beams which are steered by time delays toward candidate angles. Therefore, DOA estimation via DS beamforming is applicable for both narrowband and wideband signals. Furthermore, it is more robust to noise and sensor position errors than signal subspace methods or Fourier-based techniques [3]. However, the computational complexity of DS beamformer is $O(n^3)$ for n sensors, n steering directions, and n time snapshots.

The fast beamforming algorithm [4] incorporates a "divide-and-conquer" strategy to reduce the number of computations to $O(n^2 \log_2 n)$. Fast beamforming is a multistage algorithm in which the angular resolution of the steered beams increases as the algorithm progresses to later stages. At intermediate stages, the processed data represents partially integrated beams. Each stage of the fast beamformer splits an intermediate beam into multiple beams by steering the beam in different directions and coherently combining adjacent array elements. In effect, each stage decreases the angular spacing by steering and improves the angular resolution by partial coherent integration. In the end, the fast beamformer provides coherently integrated beams just like DS beamforming. For the application of DOA estimation, there is no need to fully integrate beams that do not contain a signal source, this paper introduces the *pruned* fast beamformer. This new method incorporates a detector that determines if there is evidence of a coherent signal source in the intermediate beams of the fast beamformer. The detector helps to further reduce computations by pruning beams that are very unlikely to include a coherent signal. In the end, fewer beams are fully formed. The energy

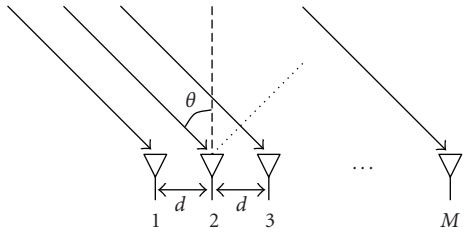

Figure 1: Geometry of the uniform linear array (ULA).

in the formed beams is used to determine whether or not a source is present at the corresponding DOA. Initial results regarding the pruned fast beamformer appeared in [5–7].

The angular accuracy of DS beamformers is not as good as the signal subspace methods that assume a finite number of signal sources. However, wideband subspace methods, such as the coherent signal subspace method (CSSM) [8], require an initial estimate of the DOAs. The output of the pruned fast beamformer can be used to initialize the CSSM. Alternatively, it can be used to determine the field-of-view (FOV) in the beamspace invariant CSSM (BI-CSSM) [9] or TOPS [10] methods. BI-CSSM requires an FOV since it takes advantage of the reduced spatial dimension. TOPS does not explicitly require an FOV [10], but an FOV can reduce computations by avoiding the calculation of condition numbers over benign regions.

This paper is organized as follows: conventional DS and fast DS beamforming are introduced in Sections 2 and 3, respectively. Then Section 4 introduces sector pruning. Section 5 discusses the computational cost of fast beamforming with and without pruning. Simulation results are provided in Section 6.

2. DELAY-AND-SUM BEAMFORMING

DS beamforming increases the signal-to-noise ratio (SNR) by coherently adding the source signal associated with a given DOA. To this end, it incorporates appropriate time delays in the output data corresponding to each sensor array element. Let $x_m(t)$ represent the output of the mth sensor, where $m = 0,\ldots,M-1$. In practice, the received signal will be discrete signal which is sampled in time. The sampling frequency should be higher than the Nyquist rate. When the sampling rate is high enough, the analytical expressions in the followings will be not so much different except for the error caused by interpolation in the process of DS beamforming. Considering fast beamforming errors which will be analyzed in detail in Section 3, we believe that the interpolation error does not change the performance significantly. Therefore, we will use continuous time signal in analysis until Section 5 where computational complexity analysis including interpolation is provided.

Given J signal sources, the output at the mth sensor is modeled as

$$x_m(t) = \sum_{j=1}^{J} s_j\left(t - l_{m,\theta_j}\right) + n_m(t), \tag{1}$$

where l_{m,θ_j} is the delay depending on the relative location of the mth sensor and DOA corresponding to the jth source θ_j. The $n_m(t)$ term represents the incoherent noise at the mth sensor, which is assumed to be both spatially and temporally White-Gaussian noise (WGN), that is,

$$\epsilon\{n_m(t)n_p(v)\} = N_0\delta(t-v)\delta(m-p), \tag{2}$$

where N_0 is the energy density of the noise and $\delta(\cdot)$ is the Dirac-delta function.

For a uniform linear array (ULA) with sensor spacing of d, the delay for a signal source at DOA θ_j is

$$l_{m,\theta_j} = \frac{md}{c}\sin\theta_j, \tag{3}$$

where c is the propagation speed through the medium (see Figure 1). The sensor spacing d should be less than the half of the wavelength of the highest frequency of the incoming signals to avoid aliasing in the spatial frequency domain. For example, when $s(t)$ is a wideband with frequency band of $[f_L, f_H]$, the sensor spacing d should be

$$d \le \frac{c}{2f_H}. \tag{4}$$

For convenience, this paper considers a ULA with M sensors so that (3) represents the delay as a function of the DOA. However, DS beamforming is applicable for any arbitrary array configuration as long as the proper delays l_{m,θ_j} are used.

To coherently integrate the source signal, the DS beamformer aligns the source signals for various steering directions, that is, hypothesized DOAs. These hypothesized DOAs, $\theta_{\mathrm{st},i}$ for $i = 0,\ldots,D-1$ can be viewed as ordered samples of a modulo-2π toroid. First, the DS beamformer forms a *steered beam* associated with the steering direction $\theta_{\mathrm{st},i}$ by delaying the signal of each sensor in order to align the phase centers and then summing up the signals spatially. Formally, this *beamformed signal* corresponding to steering direction $\theta_{\mathrm{st},i}$ is

$$z(t,\theta_{\mathrm{st},i}) = \sum_{m=0}^{M-1} a_m x_m\left(t + l_{m,\theta_{\mathrm{st},i}}\right), \tag{5}$$

where a_m is a weighting factor. For this paper, $a_m = 1$. Then the DOA estimator integrates the beamformed signal temporally to determine the energy associated with $\theta_{\mathrm{st},i}$:

$$\hat{E}_z(\theta_{\mathrm{st},i}) = \int |z(t,\theta_{\mathrm{st},i})|^2 dt. \tag{6}$$

If the steering direction $\theta_{\mathrm{st},i}$ matches the DOA of the jth source signal $s_j(\cdot)$, the summation is coherent and the corresponding energy $\hat{E}_z(\theta_{\mathrm{st},i})$ will be large. Otherwise, the summation is incoherent and the energy will be smaller. The DOA estimator then selects peaks of the energy curve that exceed a given threshold as the estimated DOAs

$$\begin{aligned}\hat{\boldsymbol{\Theta}} = \{&\theta_{\mathrm{st},i} : \hat{E}_z(\theta_{\mathrm{st},i-1}) \le \hat{E}_z(\theta_{\mathrm{st},i}),\\ &\hat{E}_z(\theta_{\mathrm{st},i+1}) \le \hat{E}_z(\theta_{\mathrm{st},i}), \hat{E}_z(\theta_{\mathrm{st},i}) > \tau\}.\end{aligned} \tag{7}$$

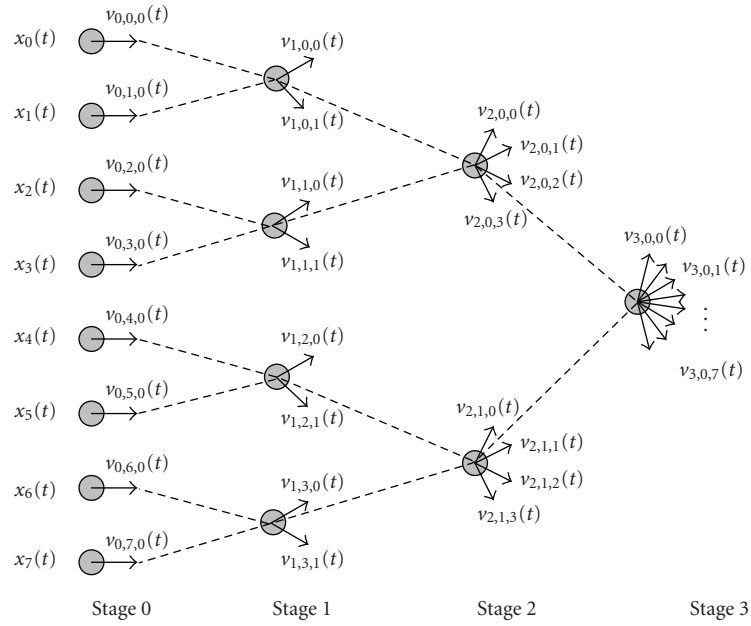

FIGURE 2: Radix-2 fast beamforming with eight sensors. At each stage, the beamforming angles are doubled and the number of sensors are halved by downsampling.

In order to estimate the DOAs accurately, one of the steering directions should match closely to one of the actual DOAs of a signal source. Usually, the steering directions are sampled uniformly in a given FOV, so the angular sample spacing should be small for accurate estimation. For a wide FOV, the number of steering directions D can be large, and as a result, the computational burden is heavy.

3. FAST MULTISTAGE DS BEAMFORMING

3.1. Fast DS beamforming

The fast DS beamforming is a divide-and-conquer method that approximates the energy curve $E_z(\theta_{\mathrm{st},i})$. It divides the angular space into small angular sectors and forms multiple partial beams per sector by partially integrating the steered signals. Initially, the entire plane forms one sector covering sources from -90° to 90°, and each of the M sensors represents a single partial beam that is not steered. The first stage of the fast beamformer divides the whole sector into R sectors. For each sector, the M partial beams are steered toward the phase center of the sectors, and L adjacent beams are integrated to form M/L partial beams by filtering and downsampling by a factor of L along the spatial (or angular) dimension. After downsampling, the number of array elements is reduced to M/L where each element corresponds to R steered partial beams. The M/L elements after downsampling, which represent the integration of L sensors, are referred to as *virtual sensors*. The phase centers for the virtual sensors are simply the centroids of the corresponding L sensors. The separation between the virtual sensors is now L times the sensor separation. The process of dividing the sectors into R subsectors, steering, filtering, and downsampling continues in an iterative fashion until each sector contains a single fully integrated beam. When R is larger than L, the total number of partial beams is increasing as the iterative processing continues. If $R = L$, the total number of partial beams remains constant throughout the whole processing. Note that R should be larger than L so it can cover the entire plane [11].

In this paper, we study a radix-2 fast beamformer, that is, $R = L = 2$, assuming that the number of sensors is $M = 2^S$. This implies that the number of steering directions is doubled and the number of virtual sensors and the number of partial beams per sector is halved at each stage. For implementation of the lowpass filter, the radix-2 fast beamformer uses a simple uniform two-tap filter. Longer filters can provide a better approximation to the DS beamformer at the expense of a higher computational cost. At stage s, the number of steering directions is 2^s and the number of steered partial beams for each direction is $M/2^s = 2^{S-s}$. Note that the steering directions are not uniformly distributed over -90° to 90° because the beam-angle centers for the sectors are uniform in the sinusoidal angular domain. The sector center for the rth sector at stage s is

$$\theta_r^{(s)} = \arcsin\left(1 - \frac{2r+1}{2^s}\right) \tag{8}$$

$$= \arcsin\left(\sum_{k=0}^{s-1} (-1)^{\lfloor 2^{k+1-s} r \rfloor} 2^{-k-1}\right) \tag{9}$$

for $r = 0, 1, \ldots, 2^s - 1$ (see Figure 3). Note that $\lfloor \beta \rfloor$ represents the largest integer that does not exceed β.

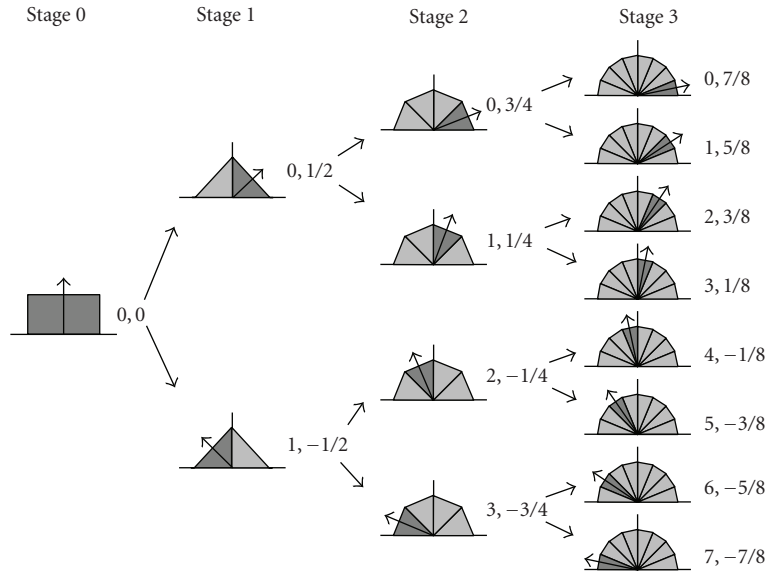

FIGURE 3: Angular support of the sectors after stages 0–3, where the numbers $r, \sin(\theta_r^{(s)})$ to the right of the support graphics represent the sector index and the sine of the center angle of the sector, respectively.

Let $v_{s,m,r}(t)$ represent the partial beam corresponding to the mth virtual sensor steered toward the rth sector after stage s. In the beginning, the mth partial beam is

$$v_{0,m,0}(t) = x_m(t) \tag{10}$$

for $m = 0, 1, \ldots, M-1$. At the initial stage ($s = 0$), each virtual sensor represents one partial beam corresponding to one sector covering the entire angular space. After the first stage ($s = 1$), the fast beamformer has performed some steering and partial integration so that the number of virtual sensors is halved. Now, each virtual sensor contains two partial beams because the number of sectors is two. Therefore, the total number of partial beams is still M. The partial beams corresponding to the mth virtual sensor are

$$\begin{aligned} &v_{1,m,0}(t) \\ &\quad = v_{0,2m,0}\left(t + \eta P_{2m}^{(0)} \sin\theta_0^{(1)}\right) + v_{0,2m+1,0}\left(t + \eta P_{2m+1}^{(0)} \sin\theta_0^{(1)}\right), \\ &v_{1,m,1}(t) \\ &\quad = v_{0,2m,0}\left(t + \eta P_{2m}^{(0)} \sin\theta_1^{(1)}\right) + v_{0,2m+1,0}\left(t + \eta P_{2m+1}^{(0)} \sin\theta_1^{(1)}\right), \end{aligned} \tag{11}$$

where $\eta = d/c$, $P_m^{(0)}$ is the location of the mth virtual sensor for stage $s = 0$, and $\theta_r^{(1)}$ is the beam-angle center of the rth sector at stage $s = 1$. According to (8), $\sin\theta_r^{(1)} = (-1)^r(1/2)$.

Since the virtual sensors are located at the centroid of two integrated virtual sensors from the previous stage, the location of the virtual sensors at stage s is given by

$$P_m^{(s)} = 2^s\left(m + \frac{1}{2}\right) - \frac{M}{2}, \tag{12}$$

for $m = 0, 1, 2, \ldots, (M/2^s) - 1$. In general, the partial beam for the mth virtual sensor output at stage s for the rth sector is computed using the partial beams from the previous stage

$$\begin{aligned} v_{s,m,r}(t) = {} & v_{s-1,2m,\lfloor 2^{-1}r \rfloor}\left(t + \frac{\eta P_{2m}^{(s-1)}(-1)^r}{2^s}\right) \\ & + v_{s-1,2m+1,\lfloor 2^{-1}r \rfloor}\left(t + \frac{\eta P_{2m+1}^{(s-1)}(-1)^r}{2^s}\right) \end{aligned} \tag{13}$$

for $r = 0, 1, \ldots, 2^{s-1} - 1$. The fast beamformer iterates (13) until $s = S$. Then the data represents one virtual sensor with 2^S fully integrated beams whose steering angles correspond to (8) or (9).

Figure 2 illustrates the partial beams and virtual sensors after each stage when $M = 8$. Before the processing begins, the eight sensors represent eight nonsteered partial beams. At stage 1, the partial beams are steered toward the beam centers of the two sectors. Then the steered partial beams of two adjacent sensors are integrated and downsampled by two. After downsampling, the virtual sensors are located at the centroid of two adjacent sensors. For the next stage, the process is repeated resulting in two virtual sensors and four sectors. Finally, after the last stage (stage 3), the data contains one virtual sensor with eight fully integrated beams. Note that the partial beams corresponding to stage s and the virtual sensor m' are determined using only the output from the "ancestor" sensors, that is, $x_m(t)$ for $m = \lfloor 2^s m' \rfloor, \ldots, \lfloor 2^s m' \rfloor + 2^s - 1$.

Figure 3 shows the location of the sector support during the first three stages of the fast beamformer. The figure also demonstrates the relationship between the sector index r and the corresponding sector center in $\sin\theta$ space. Finally,

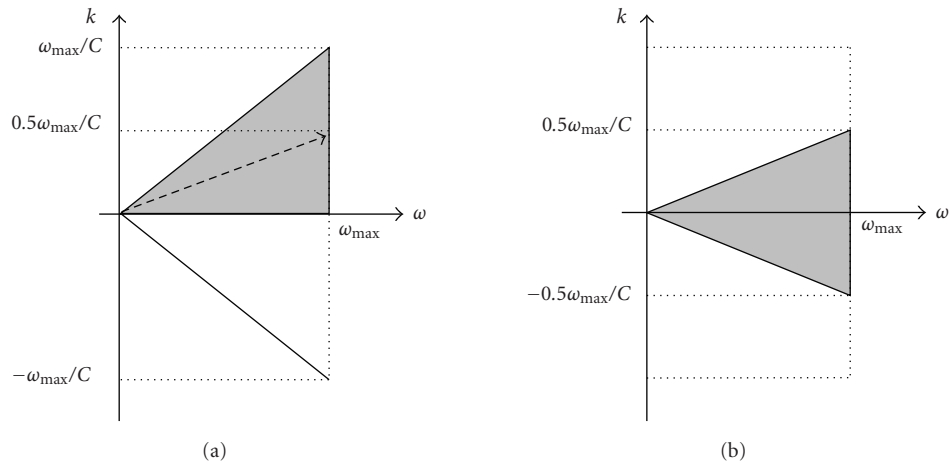

Figure 4: The spatiotemporal frequency support (k-ω) of a sector: (a) before beam steering and (b) after beam steering.

the figure illustrates that the index g corresponding to the ancestor sector at stage $s - s'$ of the rth sector at stage s is

$$g = \lfloor 2^{-s'} r \rfloor. \tag{14}$$

Figure 4 reveals why the fast beamformer works by showing the support of the sector in the k-ω frequency domain. For a linear array, the frequency support of the sensed signals $s_j(t - l_{m,\theta})$ lies in a cone whose largest spatial frequency is $k = (d/c)\omega_{\max}$, where $\omega_{\max}$ is the largest temporal frequency component in the source signals. If the DOA lies in the sector $[0, 90^\circ)$, then the sector comprises the upper part of the cone that is shaded gray in Figure 4(a). After beamsteering using (11), the spatial frequency of the sector lies within $k \in [-(d/2c)\omega, (d/2c)\omega)$. Therefore, the signal can be spatially downsampled by a factor of two. The spatial filtering, that is, the addition of adjacent virtual sensors in (11), increases the SNR by only removing noise, and the downsampling operation adjusts the frequency support of the sector back to the full cone between $k \in [-(d/c)\omega, (d/c)\omega)$ in Figure 4(a). The pruned beamforming now repeats the process with another stage of beamsteering, filtering, and downsampling using (13). As long as the spatial separation of the sensors is lower than the critical sampling threshold, the stages of the fast beamformer will improve the SNR. In Section 3.2, we characterize the processing gain by analyzing the source signal in the space-time domain.

The energy of the rth sector at stage s is

$$\hat{E}_s(r) = \frac{1}{2^{-s}M} \sum_{m=0}^{2^{-s}M-1} \frac{1}{T} \int_0^T |v_{s,m,r}(t)|^2 dt, \tag{15}$$

and this energy corresponds to the DOA $\theta_r^{(s)}$ given by (8) or (9). In the end, the energy at stage $s = S$ simplifies to

$$\hat{E}_S(r) = \frac{1}{T} \int_0^T |v_{S,0,r}(t)|^2 dt, \tag{16}$$

and $\hat{E}_S(r) \approx \hat{E}_z(\theta_r^{(S)})$. More details of the general fast DS beamformer are described in [4].

3.2. Propagation of alignment error

During each stage, the fast beamformer assumes that there is enough alignment to sum adjacent virtual sensors coherently. Once the virtual sensors are combined, the error caused by the offset between the signal direction and the sector beam-angle center becomes known. The beamforming loss can be calculated by analyzing the difference between the true and virtual sensor positions. Although the virtual sensor position is changing at each stage, the real sensor position is fixed at its position in stage zero. Therefore, the delay required for steering toward θ_0 is

$$l_{m,\theta_0} = \eta P_m^{(s)} \sin\theta_0, \tag{17}$$

and the steered beam should be

$$z(t, \theta_0) = \sum_{m=0}^{M-1} x_m(t + \eta P_m^{(0)} \sin\theta_0). \tag{18}$$

However, the partial beams are determined by recursing through (13) to be

$$v_{s,m,r}(t) = \sum_{l=0}^{2^s-1} x_{l+2^s m}\left(t + \eta \sum_{k=0}^{s-1} P^{(k)}_{\lfloor (l+2^s m)2^{-k} \rfloor} (-1)^{\lfloor 2^{-(s-1-k)} r \rfloor} 2^{-k-1}\right), \tag{19}$$

where $\eta = d/c$ and the steering direction θ_{st} is given by (9).

Assuming that the measured data contains one source signal, that is, $J = 1$, whose corresponding DOA matches the steering direction of the sector, then the partial beam simplifies to

$$v_{s,m,r}(t) = \sum_{l=0}^{2^s-1} s_0(t + e_{l,s,m,r}) + w_s(t), \tag{20}$$

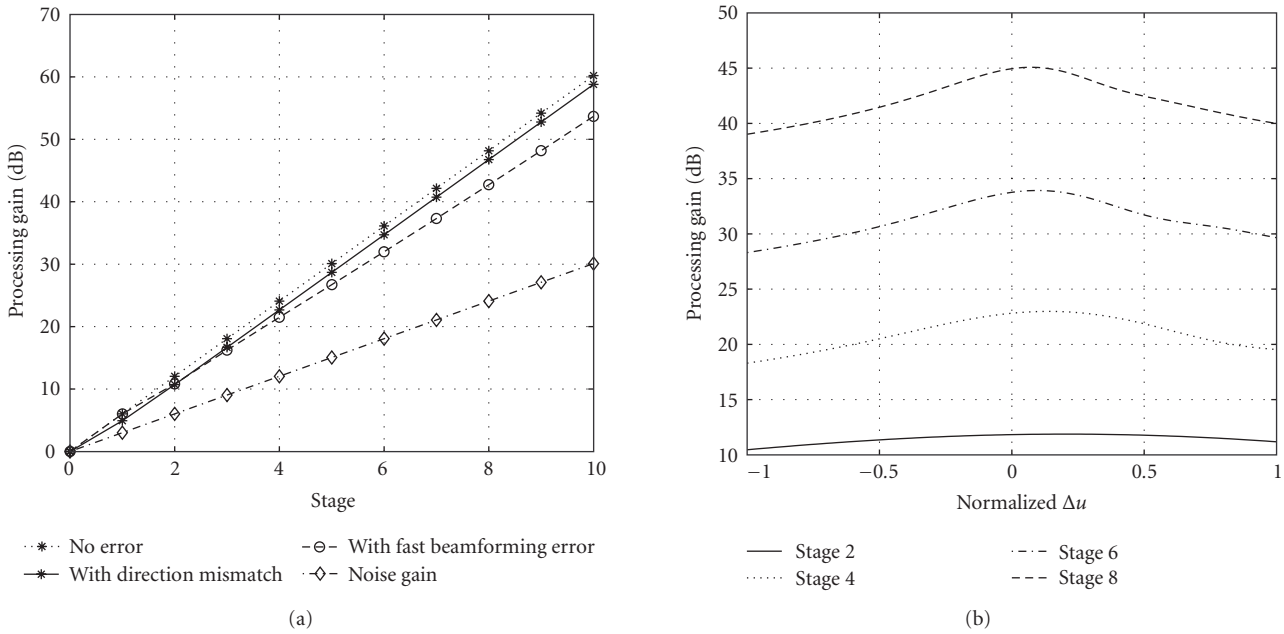

Figure 5: Processing gain (a) versus stage index s, and (b) versus the normalized position of the DOA with respect to the sector for various stages.

where $w_s(t)$ is WGN with energy density $2^s N_0$, and $e_{l,s,m,r}$ is the alignment error:

$$e_{l,s,m,r} = \eta \sum_{k=1}^{s-1} \left(P^{(k)}_{\lfloor (l+2^s m)2^{-k} \rfloor} - P^{(0)}_{l+2^s m} \right) (-1)^{\lfloor 2^{-(s-1-k)} r \rfloor} 2^{-k-1}. \tag{21}$$

When the DOA of the source signal is θ_0, the partial beam can be reexpressed as

$$v_{s,m,r}(t) = \sum_{l=0}^{2^s-1} s_0 \left(t + \eta P^{(0)}_l \Delta u + e_{l,s,m,r} \right) + w_s(t), \tag{22}$$

where $\Delta u = \sin\theta_{\text{st}} - \sin\theta_0$. Both the beamforming error $e_{l,s,m,r}$ and the steering error Δu degrade the processing gain for the signal.

Ideally, the fast beamformer would produce zero error. In the absence of error, the component of the partial beam due to the source signal is

$$v_{s,m,r} = 2^s s_0(t), \tag{23}$$

and the energy, or processing gain, of the partial beam increases as 4^s with respect to the stage index s. The noise term, $w_s(t)$, in (22) is formed by the sum of 2^s components of zero-mean WGN with variance N_0. Therefore, $w_s(t)$ is zero-mean with variance $2^s N_0$, and the processing gain of the noise component of the partial beam only increases as 2^s. The processing gain of a specific signal in the presence of errors can be calculated using (22). Figure 5(a) plots the processing gain over stages 1 through 10 for the cases of no error, beamforming error, and the worst case steering error, that is, $\Delta u = 2^{-s}$ for a sampled Sinc function of bandwidth 0.8π modulated by a sinusoid of frequency 0.6π. The impinging DOA is $\theta_0 = 20^\circ$. The plot clearly shows that the loss in processing gain due to the errors is fairly small. The processing gain of the signal component when accounting for the errors is still increasing significantly from stage to stage; and it is rising much faster than the noise component. Figure 5(b) illustrates the processing gain at various stages when accounting for both the beamforming and steering errors versus the normalized direction of the steering angle in the sector where the sector borders are ± 1. Clearly, as the stages progress, the processing gain improves. Again, the loss of processing gain due to steering error Δu is relatively small.

4. SECTOR PRUNING

4.1. Algorithm

As introduced in the previous section, fast beamforming is a multistage algorithm that refines the steered beams as it progresses from stage to stage. If a source is not present in one sector, it should be possible to avoid further processing to resolve that sector. Consequently, we propose to insert a detector between adjacent stages of the fast beamformer to determine when to stop processing in each sector. This section describes the detector needed for the pruned fast beamformer. The detector is designed to stop processing if it determines that a coherent summation has not occurred during the earlier ancestor stages. A similar detector was used in [12] for the quadtree synthetic aperture radar (SAR) processor.

Assume that the alignment error $e_{l,s,m,r}$ is zero. When the sector contains a target and its center matches the DOA ($\Delta u = 0$), then the partial beam given by (22) simplifies to

$$v_s(t) = 2^s s_0(t) + w_s(t), \tag{24}$$

where $w_s(t)$ is zero-mean WGN with variance $2^s N_0$. Note that the subscripts indicating the virtual sensor index m and the sector index r has been removed because (24) does not depend on those parameters for the case of perfect alignment.

The average energy of the partial beams for a particular sector at stage s is

$$E_s = 4^s S_0 + 2^s N_0, \tag{25}$$

where S_0 is the average signal energy:

$$S_0 = \frac{1}{T}\int_0^T |s(t)|^2 dt. \tag{26}$$

In other words, as the fast beamformer progresses, the SNR improves. We use an estimate of the SNR processing gain (SPG) as the detection statistics. This statistic is calculated for each sector after each stage. When the statistic exceeds a threshold, the sector passes the coherent signal test, and the partial beams corresponding to that sector are passed on to the next stage for refined beamforming.

The SPG estimate starts by computing the average partial beam energy $\hat{E}_s(r)$ as given by (15). Then the detection statistic t at sector r and stage s is

$$t_{s,r} = \frac{\hat{E}_s(r) - 2\hat{E}_{s-1}(\lfloor 2^{-1} r \rfloor)}{4\hat{E}_1(\lfloor 2^{-s+1} r \rfloor) - \hat{E}_2(\lfloor 2^{-s+2} r \rfloor)}. \tag{27}$$

The numerator in (27) is proportional to the estimated signal energy at the sth stage. Likewise, the denominator is proportional to the estimated noise energy at the first stage. The detection statistic is simply the estimated coherent processing gain, and the detector is

$$t_{s,r} \lessgtr 4^s \tau, \tag{28}$$

where τ is a control factor. One can adjust the control factor to balance the tradeoff between passing lower SNR sources against the computational complexity of processing noise-only sectors. Figure 6 shows the flowchart of the pruned fast beamformer. Note that the detection begins after stage 3 because the first two stages are needed to compute the denominator in (27).

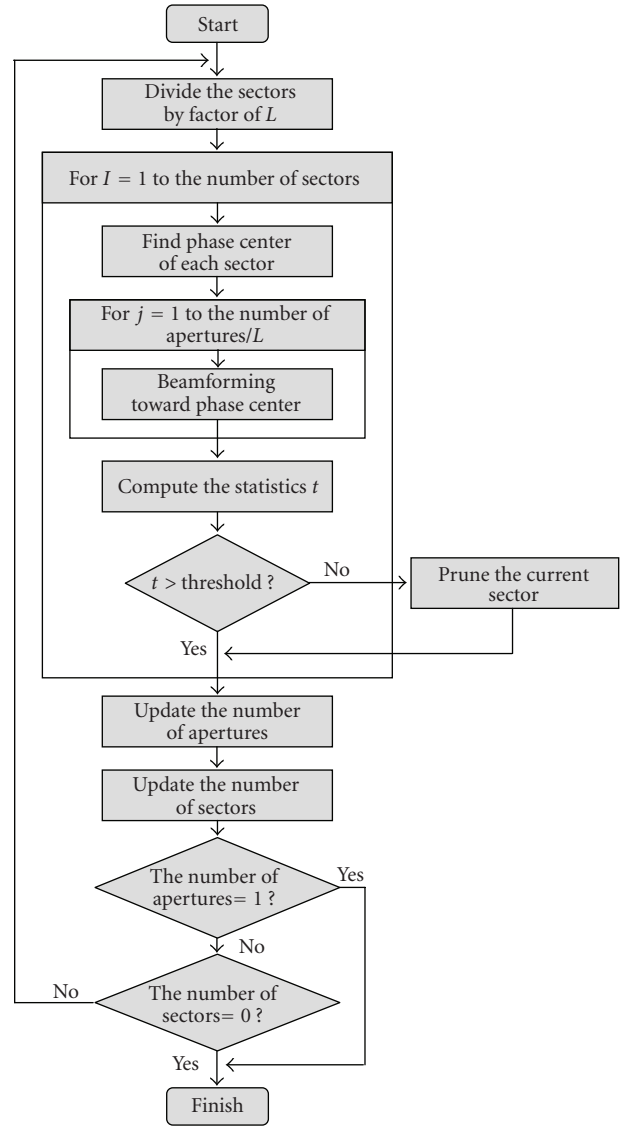

Figure 6: Flowchart of the pruned fast beamformer.

4.2. Detection performance without alignment errors

The detector performance can be summarized by receiver operator characteristic (ROC) curves. In this subsection, we consider the ideal scenario, that is, no alignment error and the steering direction matches the DOA. In practice, these assumptions are never true. For instance, the steering direction, that is, the sector beam center, changes from stage to stage. Therefore, the steering error can only be zero at one stage, and alignment errors are inevitable as discussed in Section 3.2. Section 4.3 discusses the detection performance in the presence of errors.

This subsection provides insights about the detection performance by exploiting the zero-error assumption. The derivation of the ROC curves also ignores the fact that interpolation in the fast beamforming will introduce correlation in the noise. When the ath virtual sensor at stage s is included in the bth virtual sensor at stage $s + s'$, that is, the ath virtual sensor at stage s is an ancestor of the bth virtual sensor at stage $s + s'$, then

$$\operatorname{cov}\{v_{s,a,r}(t_1), v_{s+s',b,k}(t_2)\} = 2^s N_0 \delta(t_1 - t_2) \tag{29}$$

for $r, k = 0, 1, \ldots, 2^s - 1$. When the ath virtual sensor at stage s is not an ancestor of the bth virtual sensor at stage $s + s'$, the covariance is zero because the sensors generating the two virtual sensors do not overlap and the sensor noise

is white. The covariance between energy estimates as derived in Appendix A is

$$\operatorname{cov}\{\hat{E}_s(r), \hat{E}_{s+s'}(k)\} = \frac{1}{T}\left(2^{2s+1}N_0^2 + 4\cdot 2^{3s+s'}N_0S_0\right). \quad (30)$$

Now, the coherence detector (28) is equivalent to comparing the statistic:

$$\begin{aligned}\mathcal{T}(s) = {} & E_s(r) - 2\hat{E}_{s-1}(\lfloor 2^{-1}r\rfloor) \\ & - 4^s\tau\left(4\hat{E}_1(\lfloor 2^{-s+1}r\rfloor) - \hat{E}_2(\lfloor 2^{-s+2}r\rfloor)\right)\end{aligned} \quad (31)$$

to a threshold of zero. If $\mathcal{T}(s)$ is larger than zero, the detector assumes a coherent source. The expected value of $\mathcal{T}(s)$ is

$$\varepsilon\{\mathcal{T}(s)\} = 4^s\left(2^{-1}S_0 - 4\tau N_0\right), \quad (32)$$

and Appendix B uses the covariance given by (30) to derive the variance of $\mathcal{T}(s)$ to be

$$\operatorname{var}\{\mathcal{T}(s)\} = \frac{4^sN_0^2}{T}\left[2^{s+1}\left(1 + 2^{s+7}\tau^2\right)\rho + 2\left(3\cdot 2^{2s+4}\tau^2 + 1\right)\right], \quad (33)$$

where $\rho = S_0/N_0$ is the SNR. By approximating the pdf of $\hat{E}_s(r)$ as Gaussian, $\mathcal{T}(s)$ is also Gaussian because it is a linear combination of Gaussian random variables. (The central limit theorem justifies the Gaussian assumption when the temporal integration time T is large.) As a result, the probability of detection at stage s is

$$\begin{aligned}P_d(s) &= \operatorname{Prob}\{\mathcal{T}(s) > 0 \mid S_0 > 0\} \\ &= Q\left(\frac{-\varepsilon\{\mathcal{T}(s)\}}{\sqrt{\operatorname{var}\{\mathcal{T}(s)\}}}\right),\end{aligned} \quad (34)$$

where $Q(x)$ is the error function

$$Q(x) = \frac{1}{\sqrt{2\pi}}\int_{-\infty}^{x} e^{-(1/2)x^2}dx. \quad (35)$$

The probability of false alarm at stage s can also be calculated using (34) by setting $S_0 = 0$.

4.3. Detection performance with errors

This subsection discusses the effect of errors on the detection performance. Section 3 derived the steering and alignment errors at each stage of the fast beamformer. These errors lead to a reduction of the ideal processing gain for the source signal. As shown in Figure 5, the loss varies with respect to the actual DOA and stage s. As a result, the ideal partial beam energy at stage s in (25) can be reexpressed as the actual energy via

$$\varepsilon\{\hat{E}_s\} = 4^s\alpha_s(\theta)S_0 + 2^sN_0, \quad (36)$$

where $0 < \alpha_s(\theta) < 1$ is the energy-loss factor (ELF) at stage s, and θ is the signal's DOA. The ELF is the normalized energy shown in Figure 5(b). The numerator of the detection statistic due to the signal source is

$$\begin{aligned}E_s(r) - 2E_{s-1}(\lfloor 2^{-1}r\rfloor) &= 4^s\alpha_s(\theta)S_0 - 2\cdot 4^{s-1}\alpha_{s-1}(\theta)S_0 \\ &= 4^s\left(\frac{\alpha_s(\theta)}{\alpha_{s-1}(\theta)} - \frac{1}{2}\right)\alpha_{s-1}(\theta)S_0.\end{aligned} \quad (37)$$

If α_s/α_{s-1} is less than 1/2, the detection statistic is negative and the detector will fail to detect the target. Figure 7 provides plots of α_3/α_2 and α_6/α_5 versus θ. The ELF rate varies greatly as a function of DOA. Therefore, the probability of detection depends on the signal's DOA. In general, the ELF rate never dips below the critical value of 1/2. Therefore, "on average" the detector is able to pass any coherent source at any stage as long as the threshold τ is small enough.

The ELF makes it possible to derive the expected value of $\mathcal{T}(s)$. Specifically,

$$\varepsilon\{\mathcal{T}(s)\} = 4^sN_0\left[\{\alpha_s - 0.5\alpha_{s-1} - 16\tau(\alpha_1 - \alpha_2)\}\rho - 4\tau\right]. \quad (38)$$

Note that explicit dependence of the ELF on the DOA θ is left out in the remainder of the paper for notational convenience. The variance of $\mathcal{T}(s)$ is also affected by the steering and alignment errors. The second term in (30) is derived from

$$4\cdot 2^{3s+s'}N_0S_0 = 4\cdot 2^sN_0\frac{1}{T}\int_T \varepsilon\{v_s(t)\}\varepsilon\{v_{s+s'}(t)\}dt. \quad (39)$$

Because of the alignment errors in $v_s(t)$, the integral will be less than $2^{2s+s'}S_0$, and we introduce the factor $\beta_{s,s+s'}$ such that $0 < \beta_{s,s+s'} < 1$ to model the reduction in the value of the integral. The new factor $\beta_{s,s+s'}$ depends on the stage number s, the stage displacement s', the DOA θ, and the steering direction $\hat{\theta}$. Note that β is different from α which is the energy loss in the signal due to alignment error. Then the integral is

$$\frac{1}{T}\int_T \varepsilon\{v_s(t)\}\varepsilon\{v_{s+s'}(t)\}dt = 2^{2s+s'}\beta_{s,s+s'}S_0, \quad (40)$$

and the covariance in (30) can be expressed as

$$\operatorname{cov}\{E_s, E_{s+s'}\} = \frac{1}{T}\left(2^{2s+1}N_0^2 + 4\cdot 2^{3s+s'}N_0\beta_{s,s+s'}S_0\right). \quad (41)$$

Finally, the variance is

$$\begin{aligned}&\operatorname{var}\{\mathcal{T}(s)\} \\ &\quad = \frac{2^{3s}S_0N_0}{T}\{(4\beta_{s,s} + 2\beta_{s-1,s-1} - 4\beta_{s-1,s}) \\ &\qquad + 256\cdot 2^s\tau^2(2\beta_{1,1} + \beta_{2,2} - 2\beta_{1,2}) \\ &\qquad - 128\tau(\beta_{1,s} - \beta_{2,s} - \beta_{1,s-1} + \beta_{2,s-1})\} \\ &\qquad + \frac{2\cdot 4^sN_0^2}{T}(1 + 48\cdot 4^s\tau^2).\end{aligned} \quad (42)$$

Note that (38) and (42) are the same as (32) and (33), respectively, when the values of all α and β loss factors are

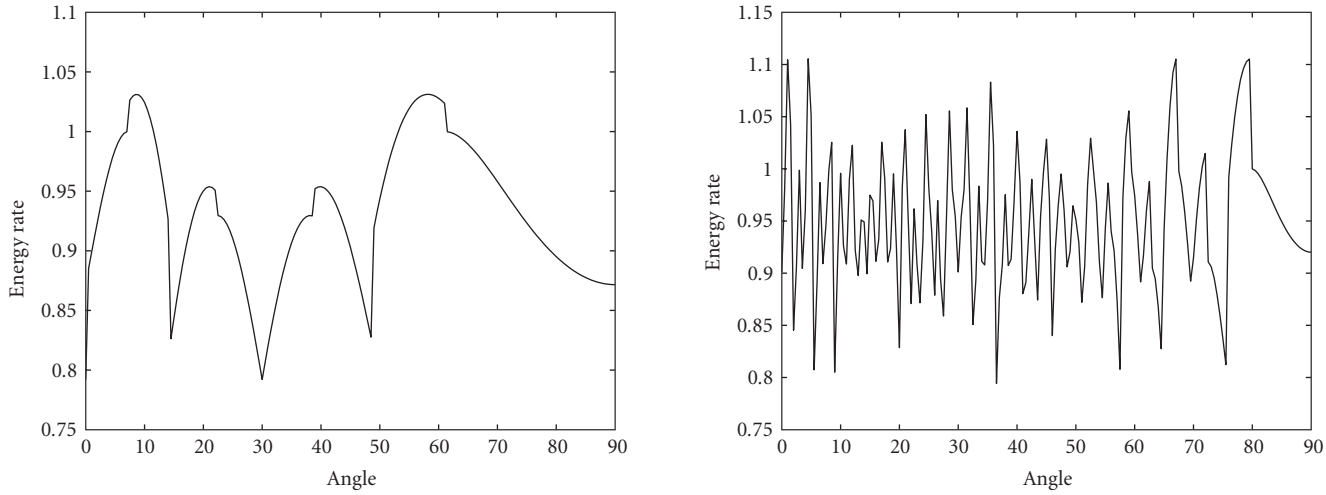

Figure 7: Energy-loss factor (ELF) rate at two consecutive stages: (a) α_3/α_2 and (b) α_6/α_5. The rates are fluctuating depending on the signal's DOA, but never become smaller than 0.5.

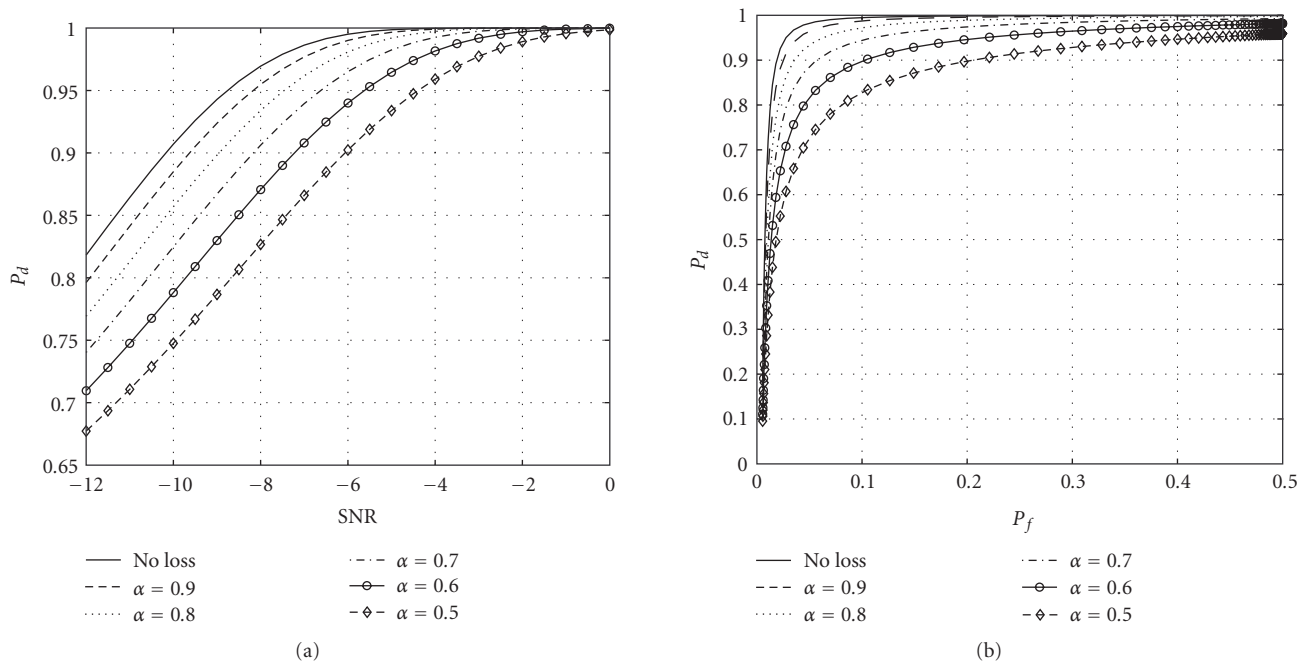

Figure 8: Detector performance at stage 3 for different values of the energy-loss factor α: (a) probability of detection versus SNR for $\tau = 0.0001$, and (b) probability of detection (P_d) versus probability of false alarm (P_f) when SNR = -4 dB. The dashed and dotted lines represent the ideal and lossy cases, respectively. In both plots the integration time is $T = 40$.

equal to one, that is, no energy losses. Now, the ROC curve can be computed from (34) as in Section 4.2.

Figure 8 shows how the energy loss reduces the detector performance by comparing the performance curves with the loss-free detector. In Figure 8(a), the threshold $\tau = 0.0001$, and in Figure 8(b), the initial SNR is -4 dB. For both plots, all the β's are set to 0.8 for the lossy cases and $s = 3$. Since the β parameters do not affect the detector performance as much as the α's, the figures show only the effect of the α's. For the "no loss" case, both the α's and β's are set to 1.0. In all plots, the solid curve represents the ideal case, and the dotted curves represent the lossy cases. As the energy loss increases, that is, α decreases, the probability of detection decreases as expected. One can see that the energy loss degrades the performance significantly. Although the results are overly pessimistic because the energy loss α is usually not as small as 0.6 in the early stages at $s = 3$, the graph shows that the detector would still work.

5. COMPUTATIONAL COMPLEXITY

The DS and fast beamformers perform two types of processing: (1) beamforming for a given DOA, and (2) computation of the beam energy. These beamformers perform the energy computation at the final stage, but the pruned fast beamformer also performs the energy computation after every stage. In addition, it also computes the detection statistic. This section details the computational complexity for the pruned and standard fast beamformers by examining the flop count for the three types of processing. It is important to note that, in practice, the sensor data is sampled at a rate of N/T so that the temporal integration is implement as a summation of N time samples.

The beamforming processing includes the timeshift, interpolation, and sensor integration. It requires three multiplications to compute the time-delay via (3). Because the beamformer is processing sampled data, the beamformer must employ interpolation, for example, bilinear interpolation, to handle noninteger sample shifts. Once the timeshift is calculated, the number of flops for processing the partial beams via (19) over N time samples is $I \cdot N + F \cdot N$, where I is the number of computations for the timeshift interpolation and F is the number for filtering, that is, summing, of adjacent beams. For a given stage, the total number of computations for beamforming is

$$D_{\text{bf}} = \{(I+F)N + 3\}B_p, \tag{43}$$

where B_p is the number of partial beams to process.

The beam energy computation calculates (15). For each partial beam, it requires N multiplies to compute the squares and $N-1$ adds for the integration. Another addition is required to accumulate the energy over the virtual sensors. The total number of computations for the energy computation is

$$D_{\text{be}} = 2NB_e, \tag{44}$$

where B_e is the number of partial beams used in the energy computation.

To obtain the detection statistics $t_{s,r}$ via (27), three floating-point operations are required: one subtraction, one multiplication, and one division. The total number of computations for the detection statistic is

$$D_{\text{ds}} = 3B_s, \tag{45}$$

where B_s is the number of sectors that are tested for potential pruning.

The total number of computations for pruned fast beamforming is

$$D_p = \{(I+F)N + 3\}B_p + 2NB_e + 3B_s. \tag{46}$$

The number of processed partial beams B_p depends on the number of source signals, the SNR, and the threshold. The maximum B_p is the same as that for conventional fast beamforming. In other words, at each stage, there are 2^{S-s} partial beams per sector and 2^s sectors for a total of $2^S = M$ partial beams. Then over the $\log_2 M$ stages, the fast beamformer processes are

$$B_{p,\max} = M \log_2 M, \tag{47}$$

partial beams. For the case of one signal source, the minimum B_p can be achieved when the fast beamformer only continues to resolve the sector containing the source after running the detection statistic. Since the pruning begins after stage 3 and continues to the final stage, the minimum B_p is

$$B_{p,\min} = 3M + \frac{M}{4}\left(1 - 0.5^{S-3}\right). \tag{48}$$

The number of partial beams used in the energy calculation B_e is the same as the total number of processed partial beams B_p when considering the pruned fast beamforming. For conventional fast beamforming, the energy calculation is necessary only during the last stage in order to identify the sectors containing a signal source. Therefore, $B_p = M$ for the conventional fast beamformer. Finally, the detection statistic operates over the sectors, and the statistic is computed from stage 3 to stage $s-1$. As a result, B_s can be as large as

$$B_{s,\max} = 8\left(2^{s-3} - 1\right), \quad \text{for } s \geq 4, \tag{49}$$

if all sectors pass the detection, or as small as

$$B_{s,\min} = 2s, \quad \text{for } s \geq 4, \tag{50}$$

if only one sector passes the detection test at each stage. Note that $B_s = 0$ for $0 \leq s \leq 3$ because the pruning only begins after the third stage. Clearly, the detection statistic is not used by the standard beamformer, where $B_s = 0$.

Overall, the minimum number of computations for the pruned fast beamformer is

$$D_{p,\min} = (I+F)NB_{p,\min} + (2N+3)B_{p,\min} + 6\log_2 M. \tag{51}$$

On the other hand, the number of computations for the nonpruned fast beamformer is

$$D_f = \{(I+F)N + 3\}M \log_2 M + M(2N-1). \tag{52}$$

When all the partial beams are passed the threshold, which is the worst case for the pruned fast beamformer, the ratio between the total number of computations of pruned fast beamformer and nonpruned fast beamformer is

$$\frac{D_{p,\max}}{D_f} \approx \frac{\{(I+F)N + 2N + 6\}M \log_2 M}{\{(I+F)N + 3\}M \log_2 M + M(2N-1)}. \tag{53}$$

When $F = 3$ and $I = 1$, which is simple bilinear interpolation and radix-2 case, and N is large, the above ratio becomes

$$\frac{D_{p,\max}}{D_f} \approx \frac{(6N+6)\log_2 M}{(4N+3)\log_2 M + (2N-1)} \approx \frac{3\log_2 M}{2\log_2 M + 1}. \tag{54}$$

As the above ratio shows, the number of computations for pruned fast beamforming is larger than that of nonpruned fast beamforming. However, it is the worst case in which

the detector does not work at all. When sectors which do not include signals are pruned, the computational saving is significant. Figure 9 shows the minimum achievable number of partial beams and the resulting number of computations used by the pruned fast beamformer normalized to the computational complexity of the standard fast beamformer when there is single signal source. Note that when the number of sensors is less than 16, the minimum number of computations for the pruned fast beamformer is larger than the number of computations for the conventional fast beamformer. This is due to the overhead incurred by computing the energy at each stage. As the number of sensors increases, the pruned fast beamformer achieves considerable computational savings as compared to the conventional fast beamformer.

6. SIMULATION AND RESULTS

6.1. Wideband signal and array model

We evaluate the utility of the pruned fast beamformer by simulating a wideband signal embedded in various realizations of complex circular Gaussian-White noise. The signal is a complex wideband signal whose magnitude is Sinc function in time domain. The frequency ranges from 0.25π to 0.5π after sampling. In other words, the bandwidth to the center frequency ratio is 2/3 and the signal is oversampled by a factor of two. The array is an ULA where the number of elements is either $M = 128$ or $M = 256$, and the sensor spacing is equal to half of the shortest wavelength so that spatial aliasing is avoided. The number of samples for temporal integration is $N = 401$. We consider single source case. Throughout the simulation the signal's DOA is -20°.

6.2. Simulations

Figure 10 illustrates the steered response of the fast beamformer at each stage with and without pruning; from left to right, stages 3 to 6 are shown. At stage 3 (left column) all sectors have been completely processed even when using pruning because the detection begins at that point. Once the detection begins between stages 3 and 4, the pruned fast beamformer is able to eliminate many sectors. By pruning sectors, the pruned beamformer processes only 8 partial beams at stage 5, and 4 partial beams at stage 6. On the other hand, the standard fast beamformer processes all 128 partial beams during all stages. The computational savings of pruning relative to full processing improves as the number of required stages, that is, $\log_2 M$, increases.

The performance of the pruned fast beamformer can be evaluated by plotting the probability of detection P_d against the computational complexity. The threshold parameter τ controls the operating condition of the detector. A low value of τ translates to a high probability that the sector containing the source signal will be fully processed. However, the low value also means that sectors containing noise have a greater probability of surviving through the processing chain. A higher threshold reduces the number of computations used to process noise-only sectors, but the probability of resolving a sector containing an actual source signal reduces. Therefore, the key ROC curve describing the performance of the pruned fast beamformer compares P_d against computational complexity under various SNR conditions.

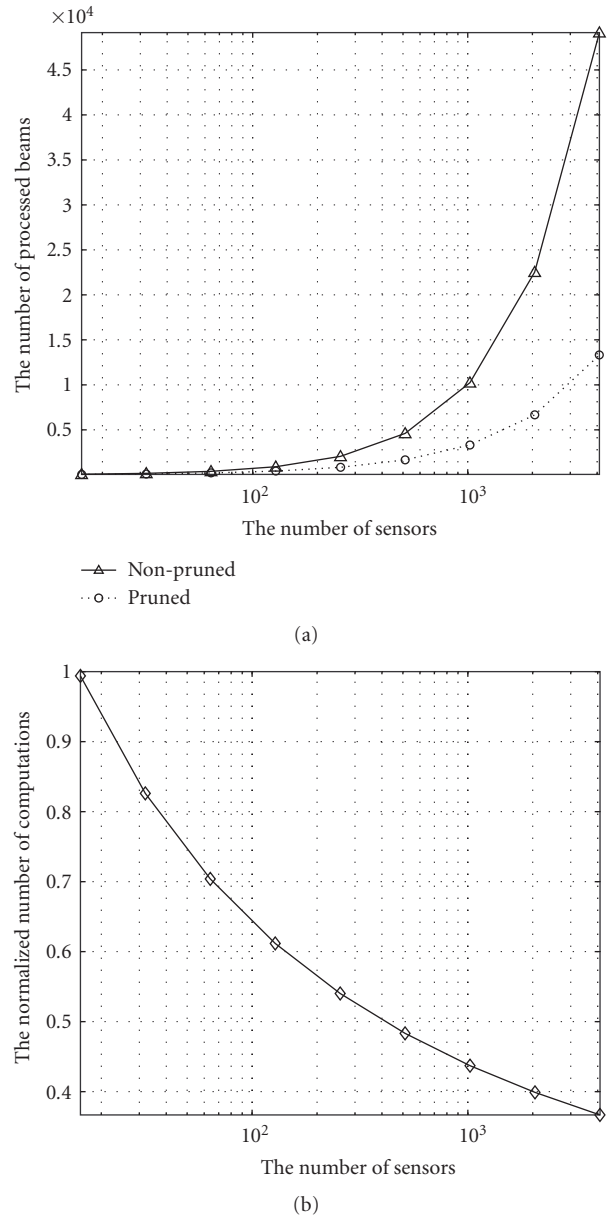

Figure 9: Computational savings of the pruned fast beamformer when single signal source is present, $N = 401, F = 3$, and $I = 1$. (a) The minimum number of processed beams for the pruned fast beamformer versus the number of processed beams for the fast beamformer, and (b) the minimum number of computations for the pruned fast beamformer normalized against the computation count for the fast beamformer.

Figure 11 shows the ROC curves for $M = 128$ and $M = 256$ by plotting P_d versus normalized computational complexity, that is, complexity of the pruned beamformer divided by that of the unpruned one. The ROC curves

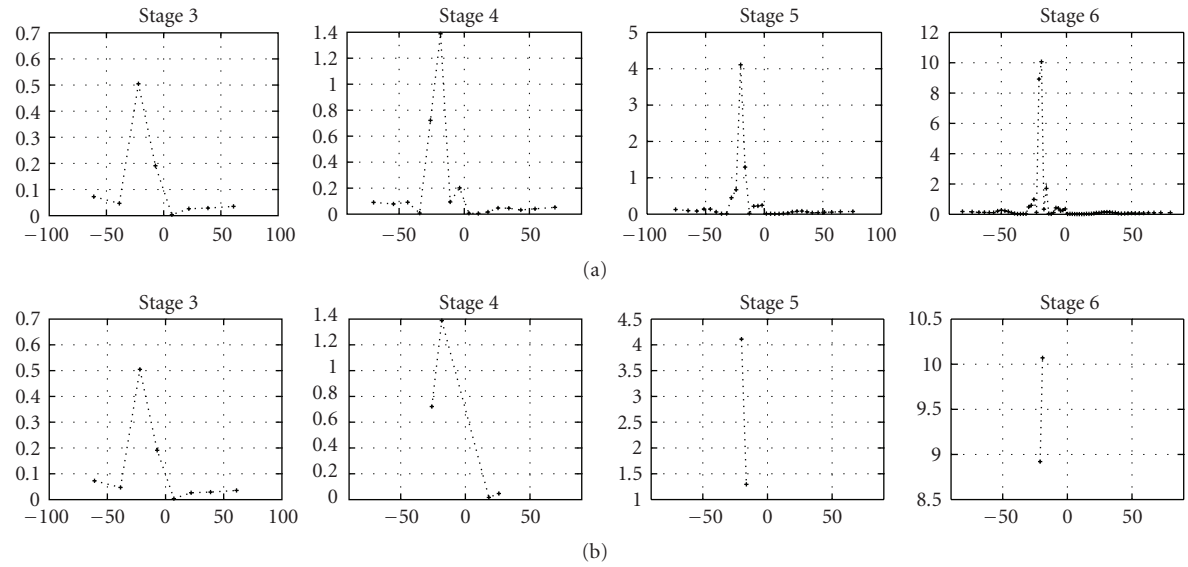

Figure 10: Steered response at each stage when the DOA is -20°. The columns from left to right represent from stage 3 to 6. The upper panels represent regular fast beamforming, while the lower panels show pruned fast beamforming.

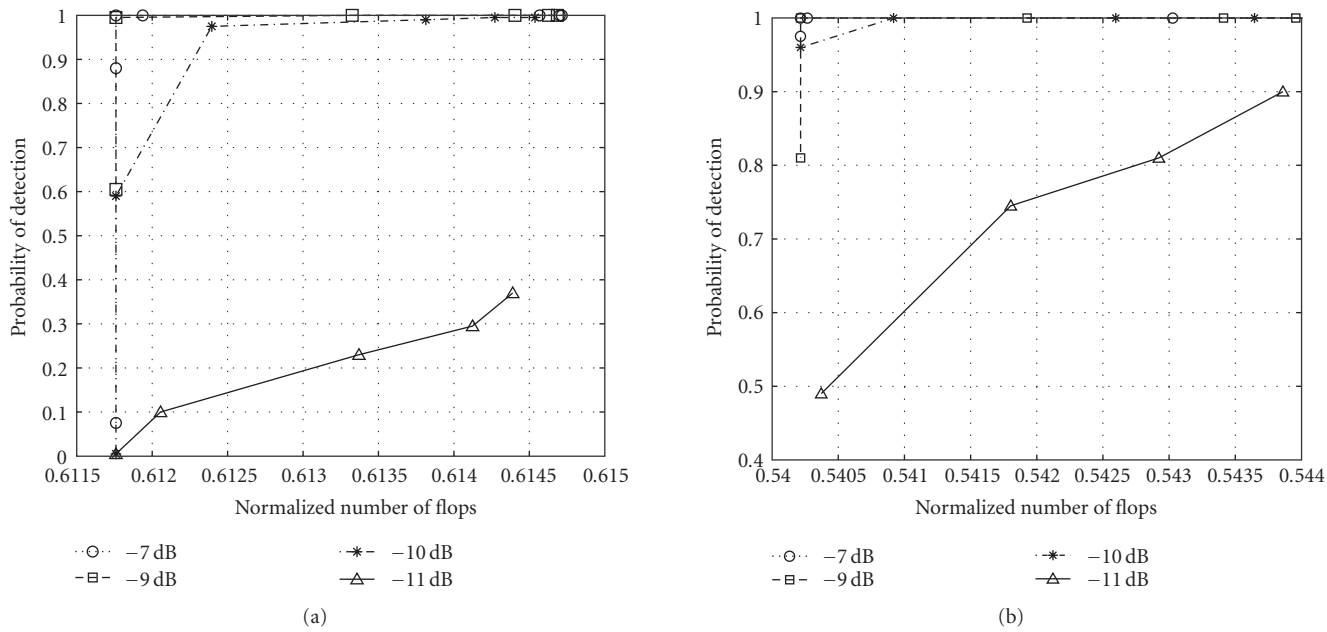

Figure 11: ROC curves. (a) $M = 128$, (b) $M = 256$.

represent SNR levels ranging from -7 dB to -11 dB, and each point on the curves was generated via 200 Monte-Carlo simulations. The computational complexity accounts for linear interpolation during beam steering and the implementation of a two-tap lowpass filter during the integration, that is, summation, of adjacent partial beams in (13).

The figure shows that the pruning detector is able to provide a high detection rate even when the computational complexity reaches its minimum value as discussed in Section 5. In fact, the minimum number of computations is achieved for a P_d close to one when the SNR is higher than -7 dB. The performance starts to drop off around -10 dB. It can be observed that the fall off in performance is consistent for the cases of $M = 128$ and $M = 256$ sensors. The only difference is that the larger array can lead to better normalized computational savings. We suspect that the consistency is due to the fact that the pruning begins after stage $s = 3$. At that stage, the SNR, after accounting for the processing gain, increases by about 9 dB independent of the value of M. It appears that as long as the signal energy is comparable to the noise energy at stage $s = 3$, the signal can easily be detected at a low false alarm rate.

Also the ability to detect the signal at that stage has major implications for the effectiveness of the pruning. As a result, as long as the initial SNR is greater than −9 dB, the pruning will be effective.

When the SNR is below −10 dB, the pruned beamformer must allow many sectors to pass the detector in order to avoid pruning the actual source signal. However, reducing the threshold τ to a value of zero does not assure that all sectors pass the detection criteria. The detection statistic given by (27) can fall below zero when the SNR is low. When this occurs, sectors containing source signals can still be pruned despite $\tau = 0$. Therefore, we conclude that the performance of the pruned fast beamformer is not very effective when the SNR is extremely low.

7. CONCLUSIONS

This paper introduces a pruning detector to the fast beamformer in order to further improve its performance. The paper also provides an error analysis of the fast beamformer and provides simulations to assess the actual performance gains of the new approach. Although the fast beamformer suffers from reduction in the processing gain achieved by the DS beamformer due to misalignment errors, the pruning detector is still effective. Specifically, the pruning is able to reduce the computational complexity while maintaining a high probability that the sector containing the source signal is fully resolved. When the number of elements of the antenna array is large so that the number of pruned sector is large, the proposed method can greatly reduce the computational burden although the pruned fast beamformer requires some computations for the detector. Another advantage of the beamformer is that it requires no initial estimate of the DOAs or the field of view (FOV). Therefore, it can be used to find initial DOAs for a number of wideband DOA estimators.

This paper focused on the radix-2 form of the pruned fast beamformer. Future work could analyze the performance of the pruned fast beamformer for various radices and sectors to find the best values (R and L) by analysis of the alignment errors. Investigation on the performance for multiple (closely spaced) sources and general array configurations is another future work to be done.

APPENDICES

A. STATISTICS FOR BEAM ENERGY

This appendix derives the statistics of the partial beam energy when assuming no steering errors. For the errorless case, the partial beam at stage s is

$$v_s(t) = 2^s s(t) + w_s(t), \tag{A.1}$$

where $s(t)$ is the signal source and $w_s(t)$ is zero-mean WGN with variance $2^s N_0$. Given that $s(t)$ and $w_s(t)$ are real-valued, the energy at stage s is

$$\begin{aligned} E_s &= \frac{1}{T}\int_T \left| v_s(t) \right|^2 dt \\ &= \frac{1}{T}\int_T \left\{2^s s(t) + w_s(t)\right\}^2 dt \\ &= \frac{2^{2s}}{T}\int_T s^2(t)dt + \frac{2^{s+1}}{T}\int_T s(t)w_s(t)dt + \frac{1}{T}\int_T w_s^2(t)dt. \end{aligned} \tag{A.2}$$

If we define the signal energy S_0 as

$$S_0 = \frac{1}{T}\int_T s^2(t)dt, \tag{A.3}$$

then the expected value of E_s is

$$\begin{aligned} \varepsilon\{E_s\} &= 4^s S_0 + \frac{2^{s+1}}{T}\int_T s(t)\varepsilon\{w_s(t)\}dt + \frac{1}{T}\int_T \varepsilon\{w_s^2(t)\}dt \\ &= 4^s S_0 + 2^s N_0. \end{aligned} \tag{A.4}$$

The covariance between energies at two different stages is nonzero when the steered beam at the earlier stage is the ancestor of a beam at the later stage. The covariance between E_s and $E_{s+s'}$ for $s' > 0$ is

$$\begin{aligned} \operatorname{cov}\{E_s, E_{s+s'}\} &= \operatorname{cov}\left\{\frac{1}{T}\int_T v_s^2(t)dt, \frac{1}{T}\int_T v_{s+s'}^2(t')dt'\right\} \\ &= \frac{1}{T^2}\iint_T \operatorname{cov}\{v_s^2(t), v_{s+s'}^2(t')\}\,dt\,dt'. \end{aligned} \tag{A.5}$$

The covariance of the partial beams squared can be simplified by exploiting the fact that

$$\operatorname{cov}\{x^2, y^2\} = 2\operatorname{cov}^2\{x, y\} + 4\operatorname{cov}\{x, y\}\varepsilon\{x\}\varepsilon\{y\}. \tag{A.6}$$

Because the partial beams at stage s and stage $s + s'$ are correlated by common sensor noise, it is easy to show that

$$\operatorname{cov}\{v_s(t), v_{s+s'}(t')\} = 2^s N_0 \delta(t - t'). \tag{A.7}$$

Then the energy covariance in (A.5) simplifies to

$$\begin{aligned} &\operatorname{cov}\{E_s, E_{s+s'}\} \\ &\quad= \frac{1}{T^2}\int_T \left\{2\left(2^s N_0\right)^2 + 4\cdot 2^s N_0 \varepsilon\{v_s(t)\}\varepsilon\{v_{s+s'}(t)\}\right\}dt \\ &\quad= \frac{1}{T}\left(2^{2s+1}N_0^2 + 4\cdot 2^{3s+s'}N_0 S_0\right). \end{aligned} \tag{A.8}$$

The energy variance, which corresponds to the case $s' = 0$, further simplifies to

$$\operatorname{var}\{E_s\} = \operatorname{cov}\{E_s, E_{s+0}\} = \frac{1}{T}\left(2^{2s+1}N_0^2 + 2^{3s+2}S_0 N_0\right). \tag{A.9}$$

B. STATISTICS FOR DETECTOR

This appendix derives the statistics used to derive the ROC performance of the pruning detector. First, we define two values:

$$\mathcal{S}(s) = E_s - 2E_{s-1}, \qquad \mathcal{N}(s) = 4E_1 - E_2, \tag{B.10}$$

which form the numerator and denominator of the detection statistic, respectively. In addition, we define

$$\mathcal{T}(s) = \mathcal{S}(s) - 4^s \tau \mathcal{N}(s). \tag{B.11}$$

When $\mathcal{T}(s)$ is larger than zero, the detector declares a target to be present; otherwise, further processing resolve the target ends. Now, one can derive the first- and second-order statistics of $\mathcal{T}(s)$ from the mean and variance of $\mathcal{S}(s)$ and $\mathcal{N}(s)$:

$$\begin{aligned}
\varepsilon\{\mathcal{S}(s)\} &= \varepsilon\{E_s\} - 2\varepsilon\{E_{s-1}\} \\
&= 4^s S_0 + 2^s N_0 - 2\left(4^{s-1} S_0 + 2^{s-1} N_0\right) = \frac{1}{2} \cdot 4^s S_0, \\
\varepsilon\{\mathcal{N}(s)\} &= 4\varepsilon\{E_1\} - \varepsilon\{E_2\} \\
&= 4(4S_0 + 2N_0) - \left(4^2 S_0 + 2^2 N_0\right) = 4N_0, \\
\operatorname{var}\{\mathcal{S}(s)\} &= \operatorname{var}\{E_s - 2E_{s-1}\} \\
&= \operatorname{var}\{E_s\} + 4\operatorname{var}\{E_{s-1}\} - 4\operatorname{cov}\{E_s, E_{s-1}\} \\
&= \frac{1}{T}\left(2^{3s+1} N_0 S_0 + 2^{2s+1} N_0^2\right), \\
\operatorname{var}\{\mathcal{N}(s)\} &= \operatorname{var}\{4E_1 - E_2\} \\
&= 16\operatorname{var}\{E_1\} + \operatorname{var}\{E_2\} - 8\operatorname{cov}\{E_1, E_2\}. \\
&= \frac{1}{T}\left(256 N_0 S_0 + 96 N_0^2\right).
\end{aligned} \tag{B.12}$$

Furthermore, the covariance between $\mathcal{S}(s)$ and $\mathcal{N}(s)$ is

$$\begin{aligned}
\operatorname{cov}\{\mathcal{S}(s)\mathcal{N}(s)\} &= \operatorname{cov}\{(E_s - 2E_{s-1}), (4E_1 - E_2)\} \\
&= 4\operatorname{cov}\{E_s, E_1\} - \operatorname{cov}\{E_s, E_2\} \\
&\quad - 8\operatorname{cov}\{E_{s-1}, E_1\} + 2\operatorname{cov}\{E_{s-1}, E_2\} = 0.
\end{aligned} \tag{B.13}$$

Therefore, the expected value of $\mathcal{T}(s)$ is

$$\varepsilon\{\mathcal{T}(s)\} = \frac{1}{2} \cdot 4^s S_0 - 4^s \tau 4 N_0 = 4^s \left(\frac{1}{2} S_0 - 4\tau N_0\right), \tag{B.14}$$

and the variance is

$$\begin{aligned}
&\operatorname{var}\{\mathcal{T}(s)\} \\
&\quad = \operatorname{var}\{\mathcal{S}(s) - 4^s \tau \mathcal{N}(s)\} \\
&\quad = \operatorname{var}\{\mathcal{S}(s)\} + 4^{2s}\tau^2 \operatorname{var}\{\mathcal{N}(s)\} - 2 \cdot 4^s \tau \operatorname{cov}\{\mathcal{S}(s), \mathcal{N}(s)\} \\
&\quad = \frac{1}{T}\left(4^s N_0^2 \left[2^{s+1}\left(1 + 2^{s+7}\tau^2\right)\rho + 2\left(3 \cdot 2^{2s+4}\tau^2 + 1\right)\right]\right),
\end{aligned} \tag{B.15}$$

where $\rho = S_0/N_0$ is the SNR.

NOTATION

θ:	Direction-of-arrival
M:	Number of sensors
N:	Number of snapshots
S:	Number of stages
J:	Number of signal sources
L:	Number of subsectors (or beams) per sector
$x_m(t)$:	Output signal at the mth sensor
$s_j(t)$:	Signal radiated from the jth source
$n_m(t)$:	Additive White-Gaussian noise at the mth sensor
$w_s(t)$:	Additive noise at stage s
$z(t, \theta)$:	Beamformed signal corresponding to steering direction θ
l_{m,θ_j}:	Time-delay depending on the relative location of the mth sensor and the DOA of the jth signal
$\theta_{\mathrm{st},i}$:	The ith steering direction
$P_m^{(s)}$:	The location of the mth virtual sensor at stage s
$e_{l,s,m,r}$:	The alignment error of the mth virtual sensor at stage s steered toward the rth sectorfor the lth REAL sensor
N_0:	Expected energy, or variance, of the additive noise $n_m(t)$
S_0:	Signal energy
d:	Sensor separation
c:	Propagation speed of the radiated signals
ω:	Temporal frequency
k:	Spatial frequency
$\epsilon\{\cdot\}$:	Expectation operator
$\hat{E}_z(\theta)$:	Energy in the beamformed signal toward steering direction θ
$\hat{E}_s(r)$:	Energy in the beamformed signal of the rth sector at stage s
Δu:	$\sin\theta_0 - \sin\theta_{\mathrm{st}}$, where θ_0 is the signal's DOA and θ_{st} is the steering direction
$\alpha_s(\theta)$:	Energy-loss factor at stage s caused by beamforming error when the signal's DOA is θ
$\beta_{s,s+s'}$:	Loss in the covariance between beamformed signals at stage s and stage $s + s'$
E_s:	Partially integrated beam energy at stage s when there is no beamforming error
$v_{s,m,r}(t)$:	Partially integrated beam corresponding to the mth virtual sensor steered toward the rth sector at stage s.

ACKNOWLEDGMENTS

This paper was prepared through collaborative participation in the Advanced Sensors and the Communications and Networks Collaborative Technology Alliances sponsored by the U.S. Army Research Laboratory under Cooperative Agreements DAAD19-01-2-008 and DAAD19-01-2-0011, respectively. The U. S. Government is authorized to reproduce and distribute reprints for government purposes notwithstanding any copyright notation thereon. The views and conclusions contained in this document are those of the authors and should not be interpreted as presenting the official policies either express or implied of the Army Research Laboratory or the U.S. Government.

REFERENCES

[1] R. Schmidt, "Multiple emitter location and signal parameter estimation," *IEEE Transactions on Antennas and Propagation*, vol. 34, no. 3, pp. 276–280, 1986.

[2] R. Roy and T. Kailath, "ESPRIT-estimation of signal parameters via rotational invariance techniques," *IEEE Transactions on Signal Processing*, vol. 37, no. 7, pp. 984–995, 1989.

[3] D. Johnson and D. Dudgeon, *Array Signal Processing: Concepts and Techniques*, Prentice-Hall, Englewood Cliffs, NJ, USA, 1993.

[4] S.-M. Oh and J. H. McClellan, "Multiresolution quadtree beamformer," in *Proceedings of the IEEE International Conference on Acoustics, Speech, and Signal Processing (ICASSP '02)*, vol. 3, pp. 2937–2940, Orlando, Fla, USA, May 2002.

[5] Y.-S. Yoon, L. M. Kaplan, and J. H. McClellan, "Pruned multi-angle resolution fast beamforming," in *Proceedings of the 2nd IEEE Sensor Array and Multichannel Signal Processing Workshop (SAM '02)*, pp. 490–494, Rosslyn, Va, USA, August 2002.

[6] Y.-S. Yoon, L. M. Kaplan, and J. H. McClellan, "Error analysis of the pruned multi-angle resolution beamformer," in *Proceedings of the 10th IEEE Digital Signal Processing Workshop and the 2nd Signal Processing Education Workshop (DSP '02)*, pp. 78–83, Pine Mountain, GA, USA, October 2002.

[7] Y.-S. Yoon, "Direction-of-arrival estimation of wideband sources using sensor arrays," Ph.D. thesis, Georgia Institute of Technology, Atlanta, Ga, USA, 2004.

[8] H. Wang and M. Kaveh, "Coherent signal-subspace processing for the detection and estimation of angles of arrival of multiple wide-band sources," *IEEE Transactions on Acoustics, Speech, and Signal Processing*, vol. 33, no. 4, pp. 823–831, 1985.

[9] T.-S. Lee, "Efficient wideband source localization using beamforming invariance technique," *IEEE Transactions on Signal Processing*, vol. 42, no. 6, pp. 1376–1387, 1994.

[10] Y.-S. Yoon, L. M. Kaplan, and J. H. McClellan, "TOPS: new DOA estimator for wideband signals," *IEEE Transactions on Signal Processing*, vol. 54, no. 6, pp. 1977–1989, 2006.

[11] S.-M. Oh and J. H. McClellan, "Multiresolution imaging with quadtree backprojection," in *Proceedings of the 35th Asilomar Conference on Signals, Systems and Computers*, vol. 1, pp. 105–109, Pacific Grove, Calif, USA, November 2001.

[12] L. M. Kaplan, J. H. McClellan, and S.-M. Oh, "Prescreening during image formation for ultra-wideband radar," *IEEE Transactions on Aerospace and Electronic Systems*, vol. 38, no. 1, pp. 74–88, 2002.